PIC-based spectroscopic chemical sensing

Tushar Sanjay Karnik[a], Jia Xu Brian Sia[b], Khoi Phuong Dao[a], Luigi Ranno[a], Juejun Hu[a,*]

[a]Department of Materials Science and Engineering, Massachusetts Institute of Technology, Cambridge, Massachusetts 02139, USA
[b]School of Electrical and Electronic Engineering, Nanyang Technological University, Singapore 639798, Singapore

ABSTRACT

Photothermal sensing is an indirect absorption sensing method that measures the change in temperature caused by the analyte molecules absorbing at a particular wavelength. While this technique has been demonstrated on various photonic platforms, silicon nitride circuits are specifically known for their ultralow propagation losses and CMOS compatibility. Here, we demonstrate suspended silicon nitride microdisk resonators that can be employed for near-infrared photothermal sensing. The photonic circuits were made in a photonic foundry multi-project wafer run with simple post-processing to remove the oxide underneath the microdisk. We observed optical bistability in our suspended microdisks, making them suitable for the required application.

Keywords: sensing, integrated photonics, spectroscopy, silicon photonics

1. INTRODUCTION

Infrared absorption sensing is a well-known technique used to probe the concentration of various substances by excitation of their vibrational modes. Photonic integrated circuits (PICs) have enabled the production of chip-scale sensors to reduce their size, weight, and power consumption (SWaP) properties. Chip-scale chemical sensors based on optical waveguides[1–21], interferometers[22–25], as well as optical resonators[26–33] have been intensively investigated. However, direct absorption-based sensing is susceptible to interference caused by scattering and reflections of molecules and waveguide roughness[2]. Alternatively, photothermal sensing (PTS) is an indirect technique that measures the rise in temperature from the absorption of a pump laser by monitoring the shift in the cavity resonant wavelength of the probe laser.

PTS has been demonstrated on several photonic platforms, including silicon-on-insulator (SOI)[34], thin-film lithium niobate (TFLN)[35], chalcogenide glasses[36], and silicon nitride[37]. Theoretical calculations show that the PTS enhancement factor, defined as the ratio of change in power of the probe beam to the pump beam, is proportional to the Q-factor of the resonant cavity[30,38]. Silicon nitride photonics have demonstrated remarkably low loss and high-Q resonators exceeding 100 million[39,40], making them a suitable candidate for PTS. Moreover, silicon nitride is CMOS compatible and is included in the process design kit (PDK) of major PIC foundries. Additionally, suspended structures have shown improved sensitivity for PTS owing to their lower thermal conductivity. Among the photonic components employed for PTS, microdisks can be easily suspended by anchoring them with bottom cladding around the center, which does not overlap with the optical mode residing near the disk edge.

Here, we report a suspended silicon nitride microdisk resonator fabricated using a multi-project wafer (MPW) run by AIM Photonics foundry[41]. The microdisk was characterized both before and after the suspension process. We discuss the chip design and post-processing steps required to suspend the microdisk.

2. DESIGN OF MICRODISK RESONATOR

The microdisk was designed on a passive low-loss silicon nitride (SiN) PDK offered by AIM Photonics. Figure 1(a) shows the wafer stack profile consisting of two 220 nm SiN layers separated by 100 nm silica. The top nitride layer serves as an etch stop for removing the top oxide to create the sensing trench. This sensing trench was placed on all the microdisks to enable interaction of the evanescent field with analyte species and to undercut the bottom oxide via wet etching. According

*hujuejun@mit.edu; phone 1-302-766-3083

to the design rules, the minimum dimension of the sensing trench should be 100 µm. Therefore, we designed waveguide crossings to act as anchors after the long bus waveguide was fully suspended, as shown in Figures 1(b) and 1(c).

The waveguide crossing dimensions were calculated using the particle swarm optimization algorithm in the Lumerical FDTD solver. Phase matching of the bus waveguide and microdisk resonator fundamental mode is essential to prevent the excitation of higher-order microdisk modes. According to Figure 1(d), the waveguide width and disk radius were chosen to match the effective index of their respective fundamental modes. We designed two microdisks with radii and bus waveguide widths of 65/95 µm and 2/2.25 µm, respectively. The coupling gap for the 65 µm disk was kept at 150/300/450 nm, and for the 95 µm disk, it was kept at 100/200/300/400/500 nm. The bus waveguide was point-coupled to the disk, as pulley coupling would become mechanically unstable after suspension.

The effective indices were calculated using Lumerical MODE simulations for suspended structures with no bottom oxide cladding. The waveguide width for routing was kept standard at 1.5 µm, and circular bends with a 95 µm radius were used, as recommended by AIM Photonics. To adiabatically transition to the bus waveguide width, a 30 µm linear taper was used in the region with top oxide cladding. 200 µm inverse tapers with a 475 nm tip width were used as edge couplers. All the components were designed for transverse electric (TE) polarization.
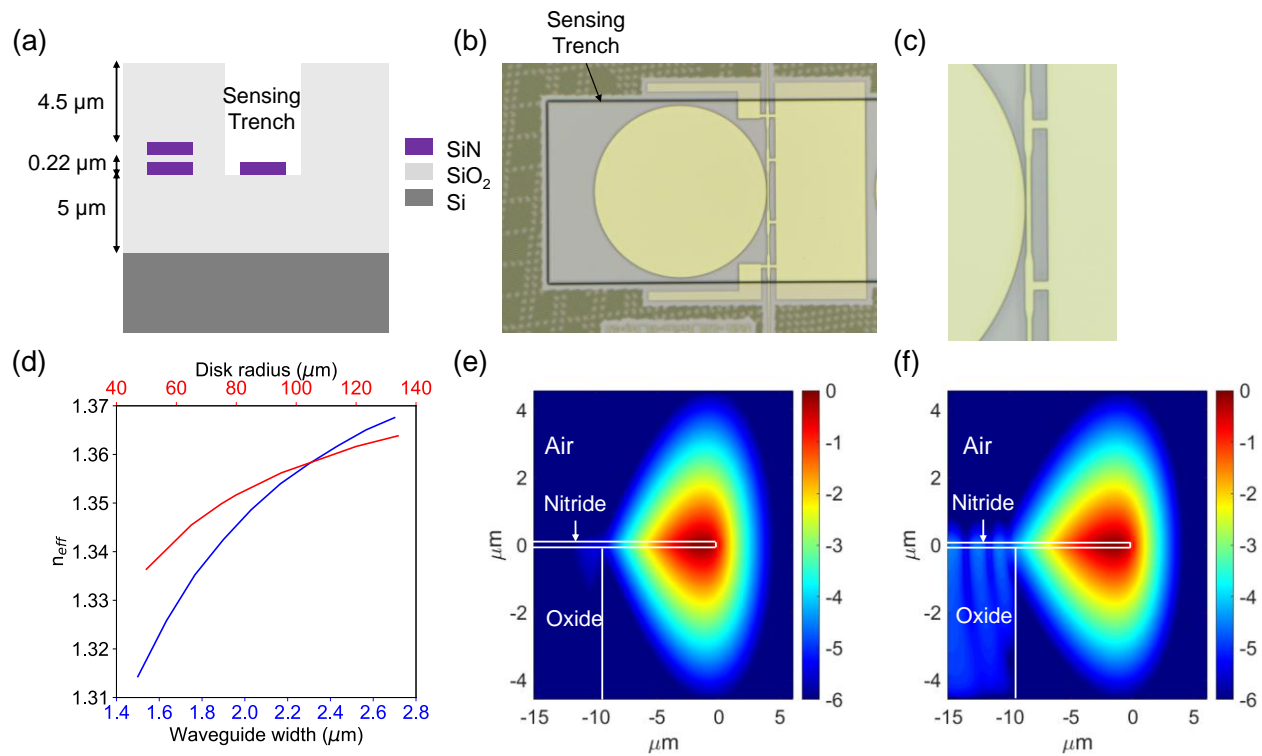

Figure 1. (a) Stack profile of AIM passive low-loss nitride PDK. (b) Microscope image of the fabricated microdisk resonator with radius = 95 µm and coupling gap = 500 nm. (c) Magnified view of the coupling region. (d) The simulated effective index of the fundamental mode in waveguide (blue-line) and microdisk (red-line). Simulated electric field intensity for the microdisk fundamental mode for disk radius equal to (e) 65 µm and (f) 95 µm plotted on a log scale. The origin represents the disk perimeter.

3. FABRICATION OF SUSPENDED MICRODISK

The chips received from AIM Photonics still had bottom oxide (BOX) cladding for the microdisks. To improve the thermal conductivity, we aimed to remove the oxide by using buffered oxide etch (BOE)[42]. Both our simulations and optical measurements indicated that approximately 9.5 µm of undercut is required to minimize leakage of the microdisk fundamental mode into the BOX, which could result in high propagation losses. The entire post-processing process is depicted in Figure 2. First, the entire chip except for the sensing trenches was protected with negative photoresist using direct laser write lithography. The chip was then placed between two Si pieces bonded to a carrier wafer using a photoresist.

A thick photoresist AZ 10XT was carefully dropped on the chip edges using a micropipette to prevent it from flowing into the sensing trenches. Finally, the whole assembly was baked at 110 °C for 20–30 minutes until the thick resist hardened. The carrier wafer was placed in an undiluted 7:1 BOE solution for 95 minutes to undercut 9.5 µm of oxide. After rinsing the wafer in DI water, the chip was immediately transferred to isopropanol without letting it dry. Lastly, the chip was subjected to critical point drying to avoid damage to the suspended structures.
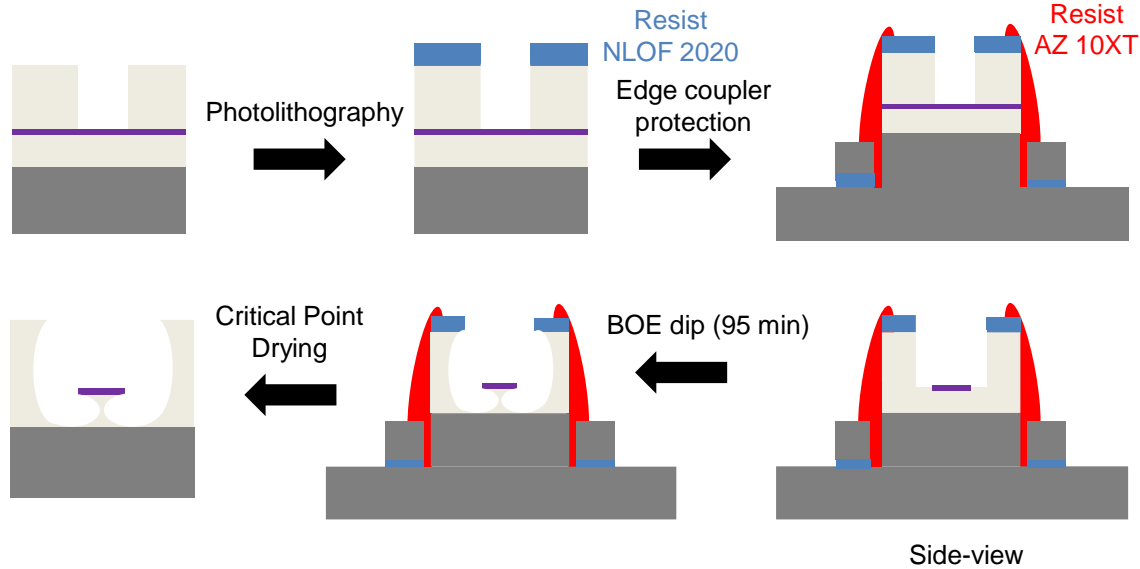

Figure 2. Process flow for suspending the microdisk resonators

4. RESULTS AND DISCUSSION

The microdisks' optical response was measured both before and after the suspension. An optical vector analyzer (OVA, Luna Innovations Inc.) with a built-in external cavity tunable laser was used as the interrogation light source, in conjunction with an erbium-doped fiber amplifier (Amonics Ltd.). The light was coupled in and out of the chip using lensed fibers. Figures 3(a) and 3(d) show the measured microdisk transmission before the suspension for a disk radius of 95 µm and 65 µm, respectively. We observed that the critical coupling condition for the 95 µm disk radius was met around a coupling gap between 400–500 nm, featuring a Q factor of more than 300,000. The propagation loss was estimated between 0.5–0.7 dB/cm. The calculated group index (n_g) from the measured free spectral range (FSR) was 1.742, which closely matched the simulated n_g of 1.758 for the fundamental mode. Radiation losses estimated from the simulations were approximately 0.2 dB/cm due to leakage into the BOX. Figure 3(a) shows the transmission of a highly overcoupled microdisk with a 100 nm coupling gap. We also observed secondary peaks in the spectrum originating from the second-order mode, as its effective index ($n_{eff} = 1.45$) was very close to that of the fundamental mode ($n_{eff} = 1.48$). These secondary peaks were not as prominent due to the high radiation losses (~20 dB/cm) calculated by simulations. For the 65 µm disk radius, the critical coupling could not be achieved even for a small coupling gap of 150 nm, as shown in Figure 3(d). With a Q-factor of 20k–30k, the propagation loss was estimated between 6–8 dB/cm. The measured n_g (1.726) closely matched the simulated n_g (1.748) for the fundamental mode. The simulated radiation losses were 6 dB/cm. We did not observe any secondary peaks in the transmission as the radiation loss for the second-order mode was extremely high (~200 dB/cm).

For suspending the microdisk resonators, we etched the chip in BOE for 35 min, 60 min, and 95 min to undercut approximately 3.5 µm, 6 µm, and 9.5 µm of BOX, respectively. However, no resonant peaks were observed for 3.5 µm and 6 µm etch. We hypothesize that this is due to the mode field overlapping significantly with the undercut BOX/Air interface with high surface roughness. We detected the resonant peaks only after 9.5 µm etch, as shown in Figures 3(b) and 3(c) for disk radii equal to 95 µm and 65 µm, respectively. Even though BOE has a high selectivity for silica compared to SiN, we observed that the nitride layer was also etched to some extent. Figures 3(c) and 3(f) show the SEM images of the coupling region taken after the 9.5 µm undercut. In the case of a 95 µm disk radius, the coupling gap increased from 400 nm to 600 nm, and the waveguide width was reduced from 2.25 µm to 2.11 µm. Similarly, for the 65 µm disk radius, the coupling gap increased from 150 nm to 330 nm, and the waveguide width was reduced from 2 µm to 1.86 µm. This

implied that roughly 70 nm of SiN was etched from the sides. The measured ng for 95 µm and 65 µm microdisk after suspension were 1.60 and 1.59, which corresponded to a nitride thickness between 150–160 nm according to simulations. Hence, the reduction in thickness was between 60–70 nm.

Around the 1550 nm wavelength, the peak extinction of the 95 µm and 65 µm microdisk resonators was approximately -1 dB and -5 dB, respectively. Moreover, these peaks only appeared for the smallest coupling gaps in both cases. We estimated the propagation loss of the fundamental mode to be around 8 dB/cm and 2 dB/cm for 95 µm and 65 µm disk radius, respectively. These results are opposite to the values obtained before the suspension. Before the suspension, radiation loss was the major contributor to the overall losses in the microdisk, whereas after the suspension, the primary cause of loss arises from the field overlapping with the rough BOX/Air interface. This can also be observed in Figures 1(e) and 1(f), which show the electric field intensity of the fundamental mode on a log scale after undercutting 9.5 µm of oxide. The field overlaps more in the case of the 95 µm disk radius compared to the 65 µm one. The simulations indicate that the 95 µm disk is more susceptible to losses due to the BOX/Air interface, which agrees with our measured values.

The optical characterization indicated that the microdisk design with a starting radius of 65 µm and a 150 nm coupling gap yielded promising resonant peaks after the suspension and was suitable for performing PTS. Figure 4(a) shows the microscope image of a microdisk after suspension. The color change near the circumference of the disk indicates that the BOX underneath has been etched.
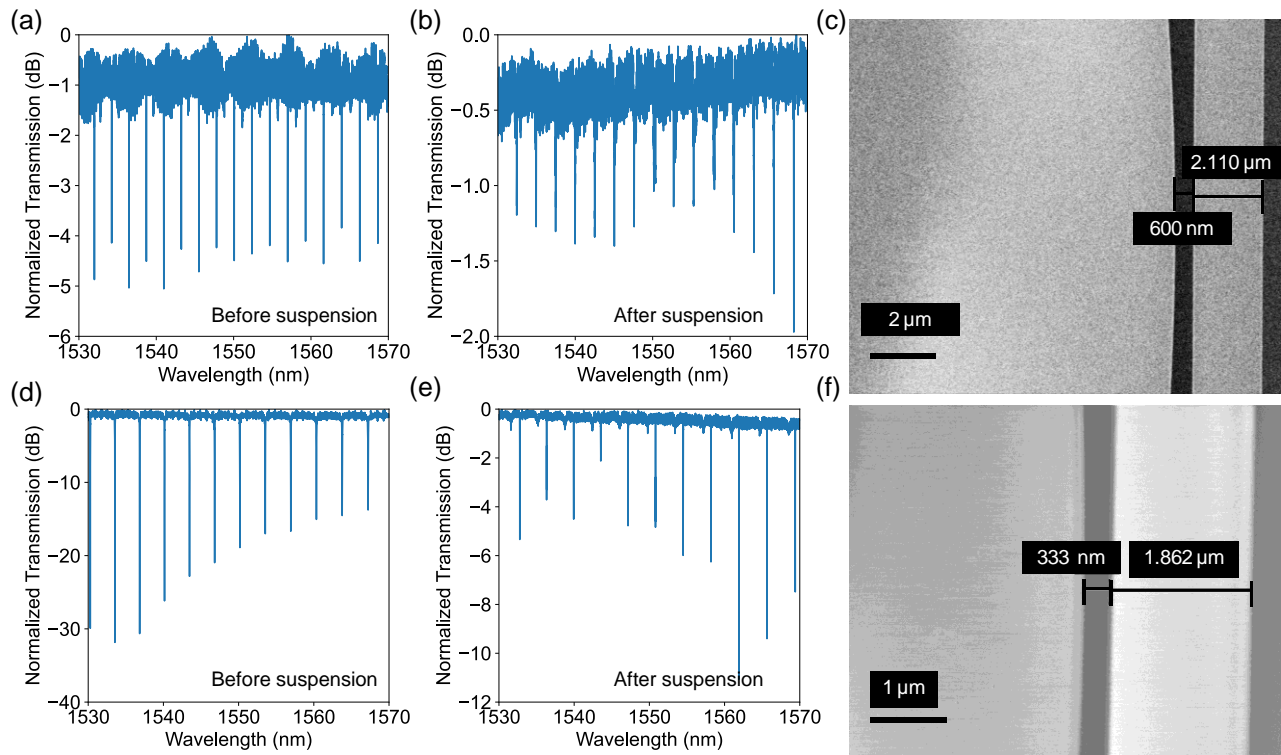

Figure 3. Normalized transmission vs. wavelength for microdisk resonator with radius = 95 µm and coupling gap = 100 nm (a) before suspension and (b) after suspension. (c) SEM image of the microdisk with radius = 95 µm and coupling gap = 100 nm taken after suspension. Normalized transmission vs. wavelength for microdisk resonator with radius = 65 µm and coupling gap = 150 nm (a) before suspension and (b) after suspension. (c) SEM image of the microdisk with radius = 65 µm and coupling gap = 150 nm taken after suspension.

We tested the photothermal properties of the microdisk by pumping the chip with increasing optical power. The laser was red-scanned from a wavelength of 1530–1570 nm. Before the suspension, we only observed a redshift in the resonant wavelength, as shown in Figure 4(b). In contrast, after the suspension, we observed optical bistability (see Figure 4(c)), which can be attributed to the reduced thermal conduction of the system. This showcases the importance of removing the BOX for PTS.
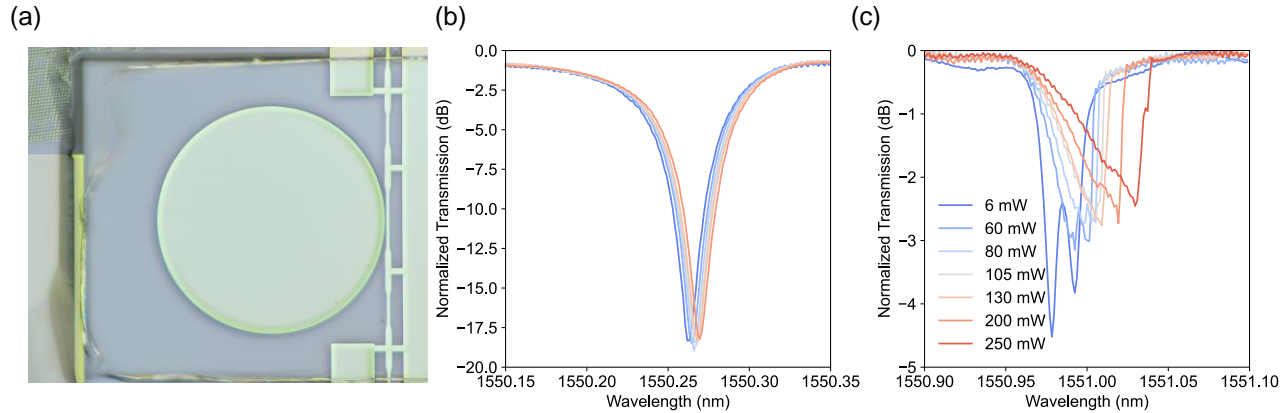
Figure 4. (a) Microscope image of microdisk resonator after suspension. Normalized transmission of microdisk resonator with radius = 65 µm and coupling gap = 150 nm for increasing input power (b) before suspension and (b) after suspension.

5. CONCLUSIONS

In summary, we have demonstrated a successful fabrication of microdisk resonators through a photonic foundry MPW run. Our measurement results indicated that the suspended microdisks can be used in performing PTS owing to their superior heat retention properties. Since SiN also gets attacked by BOE while removing the BOX, we aim to reduce the etch time while minimizing the mode field overlap with the BOX/Air interface. Therefore, we conclude that a SiN microdisk with a 30–65 µm radius will perform better despite the higher radiation losses.

REFERENCES

[1] Jokerst, N.M., Luan, L., Palit, S., Royal, M., Dhar, S., Brooke, M.A., and Tyler, T., "Progress in chip-scale photonic sensing," IEEE Transactions on Biomedical Circuits and Systems 3(4), 202–211 (2009).

[2] Veldhuis, G.J., Parriaux, O., Hoekstra, H.J.W.M., and Lambeck, P. V., "Sensitivity Enhancement in Evanescent Optical Waveguide Sensors," Journal of Lightwave Technology 18(5), 677–682 (2000).

[3] Lukosz, W., "Integrated optical chemical and direct biochemical sensors," Sensors and Actuators B: Chemical 29(1–3), 37–50 (1995).

[4] Su, P., Han, Z., Kita, D., Becla, P., Lin, H., Deckoff-Jones, S., Richardson, K., Kimerling, L.C., Hu, J., et al., "Monolithic on-chip mid-IR methane gas sensor with waveguide-integrated detector," Applied Physics Letters 114(5), 051103 (2019).

[5] Han, Z., Lin, P., Singh, V., Kimerling, L., Hu, J., Richardson, K., Agarwal, A., and Tan, D.T.H.H., "On-chip mid-infrared gas detection using chalcogenide glass waveguide," Applied Physics Letters 108(14), 141106 (2016).

[6] Densmore, A., Xu, D.X., Waldron, P., Janz, S., Cheben, P., Lapointe, J., Delâge, A., Lamontagne, B., Schmid, J.H., et al., "A silicon-on-insulator photonic wire based evanescent field sensor," IEEE Photonics Technology Letters 18(23), 2520–2522 (2006).

[7] Liu, Q., Manel Ramirez, J., Vakarin, V., Roux, X. LE, Ballabio, A., Frigerio, J., Chrastina, D., Isella, G., Bouville, D., et al., "Mid-infrared sensing between 5.2 and 6.6 um wavelengths using Ge-rich SiGe waveguides [Invited]," Optical Materials Express 8(5), 1305–1312 (2018).

[8] Hu, J., Tarasov, V., Agarwal, A., Kimerling, L., Carlie, N., Petit, L., and Richardson, K., "Fabrication and testing of planar chalcogenide waveguide integrated microfluidic sensor," Optics Express 15(5), 2307 (2007).

[9] Alberti, S., Datta, A., and Jágerská, J., "Integrated Nanophotonic Waveguide-Based Devices for IR and Raman Gas Spectroscopy," Sensors 21(21), 7224 (2021).

[10] Wang, P., and Miller, B.L., "Waveguide-Enhanced Raman Spectroscopy (WERS): An Emerging Chip-Based Tool for Chemical and Biological Sensing," Sensors 22(23), 9058 (2022).

[11] Vlk, M., Datta, A., Alberti, S., Yallew, H.D., Mittal, V., Murugan, G.S., and Jágerská, J., "Extraordinary evanescent field confinement waveguide sensor for mid-infrared trace gas spectroscopy," Light: Science & Applications 10, 26 (2021).

[12] Ettabib, M.A., Marti, A., Liu, Z., Bowden, B.M., Zervas, M.N., Bartlett, P.N., and Wilkinson, J.S., "Waveguide Enhanced Raman Spectroscopy for Biosensing: A Review," ACS Sensors 6(6), 2025–2045 (2021).

[13] Kita, D., Michon, J., and Hu, J., "A packaged, fiber-coupled waveguide-enhanced Raman spectroscopic sensor," Optics Express 28(10), 14963–14972 (2020).

[14] Tyndall, N.F., Stievater, T.H., McGill, R.A., Koo, K., Kozak, D.A., Pruessner, M.W., Rabinovich, W.S., and Holmstrom, S.A., "Waveguide-enhanced Raman spectroscopy of trace chemical warfare agent simulants," Optics Letters 43(19), 4803–4806 (2018).

[15] Turk, N., Raza, A., Wuytens, P., Demol, H., Daele, M. Van, Detavernier, C., Skirtach, A., Gevaert, K., and Baets, R., "Waveguide-based surface-enhanced Raman spectroscopy detection of protease activity using non-natural aromatic amino acids," Biomedical Optics Express 11(8), 4800–4816 (2020).

[16] Holmstrom, S.A., Stievater, T.H., Kozak, D.A., Pruessner, M.W., Tyndall, N., McGill, R.A., Rabinovich, W.S., and Khurgin, J.B., "Trace gas Raman spectroscopy using functionalized waveguides," Optica 3(8), 891–896 (2016).

[17] Dhakal, A., Wuytens, P.C., Peyskens, F., Jans, K., Thomas, N. Le, and Baets, R., "Nanophotonic Waveguide Enhanced Raman Spectroscopy of Biological Submonolayers," ACS Photonics 3(11), 2141–2149 (2016).

[18] Coucheron, D.A., Wadduwage, D.N., Murugan, G.S., So, P.T.C., and Ahluwalia, B.S., "Chip-Based Resonance Raman Spectroscopy Using Tantalum Pentoxide Waveguides," IEEE Photonics Technology Letters 31(14), 1127–1130 (2019).

[19] Raza, A., Clemmen, S., Wuytens, P., Muneeb, M., Van Daele, M., Dendooven, J., Detavernier, C., Skirtach, A., and Baets, R., "ALD assisted nanoplasmonic slot waveguide for on-chip enhanced Raman spectroscopy," APL Photonics 3(11), 116105 (2018).

[20] Dhakal, A., Wuytens, P., Peyskens, F., Thomas, N. Le, Subramanian, A.Z., and Baets, R., "Evanescent excitation and collection of spontaneous Raman spectra using silicon nitride nanophotonic waveguides," Optics Letters 39(13), 4025–4028 (2014).

[21] Zhao, H., Clemmen, S., Raza, A., and Baets, R., "Stimulated Raman spectroscopy of analytes evanescently probed by a silicon nitride photonic integrated waveguide," Optics Letters 43(6), 1403–1406 (2018).

[22] Ranno, L., Tan, Y.Z., Ong, C.S., Guo, X., Koo, K.N., Li, X., Wang, W., Serna, S., Liu, C., et al., "Crown ether decorated silicon photonics for safeguarding against lead poisoning," Nature Communications 15, 3820 (2024).

[23] Jobst, G., Petrou, P.S., Botsialas, A., Kakabakos, S.E., Oikonomou, P., Salapatas, A., Tukkiniemi, K., Sopanen, M., Misiakos, K., et al., "All-silicon monolithic Mach-Zehnder interferometer as a refractive index and bio-chemical sensor," Optics Express 22(22), 26803–26813 (2014).

[24] Liu, Q., Tu, X., Kim, K.W., Kee, J.S., Shin, Y., Han, K., Yoon, Y.J., Lo, G.Q., and Park, M.K., "Highly sensitive Mach–Zehnder interferometer biosensor based on silicon nitride slot waveguide," Sensors and Actuators B: Chemical 188, 681–688 (2013).

[25] Ymeti, A., Greve, J., Lambeck, P. V., Wink, T., Van Novell, S.W.F.M., Beumer, T.A.M., Wijn, R.R., Heideman, R.G., Subramaniam, V., et al., "Fast, ultrasensitive virus detection using a young interferometer sensor," Nano Letters 7(2), 394–397 (2007).

[26] Iqbal, M., Gleeson, M.A., Spaugh, B., Tybor, F., Gunn, W.G., Hochberg, M., Baehr-Jones, T., Bailey, R.C., and Gunn, L.C., "Label-free biosensor arrays based on silicon ring resonators and high-speed optical scanning instrumentation," IEEE Journal on Selected Topics in Quantum Electronics 16(3), 654–661 (2010).

[27] Ksendzov, A., and Lin, Y., "Integrated optics ring-resonator sensors for protein detection," Optics Letters 30(24), 3344–3346 (2005).

[28] Sun, Y., and Fan, X., "Optical ring resonators for biochemical and chemical sensing," Analytical and Bioanalytical Chemistry 399(1), 205–211 (2011).

[29] Hu, J., Carlie, N., Petit, L., Agarwal, A., Richardson, K., and Kimerling, L.C., "Cavity-enhanced ir absorption in planar chalcogenide glass microdisk resonators: Experiment and analysis," Journal of Lightwave Technology 27(23), 5240–5245 (2009).

[30] Hu, J., "Ultra-sensitive chemical vapor detection using micro-cavity photothermal spectroscopy," Optics Express 18(21), 22174 (2010).

[31] Chen, Y., Lin, H., Hu, J., and Li, M., "Heterogeneously Integrated Silicon Photonics for the Mid-Infrared and Spectroscopic Sensing," ACS Nano 8(7), 6955–6961 (2014).

[32] Lin, H., Yi, Z., and Hu, J., "Double resonance 1-D photonic crystal cavities for single-molecule mid-infrared photothermal spectroscopy: theory and design," Optics Letters 37(8), 1304 (2012).

[33] Chao, C.Y., Fung, W., and Guo, L.J., "Polymer microring resonators for biochemical sensing applications," IEEE Journal on Selected Topics in Quantum Electronics 12(1), 134–142 (2006).

[34] Vasiliev, A., Malik, A., Muneeb, M., Kuyken, B., Baets, R., and Roelkens, G., "On-Chip Mid-Infrared Photothermal Spectroscopy Using Suspended Silicon-on-Insulator Microring Resonators," ACS Sensors 1(11), 1301–1307 (2016).

[35] Yan, Y., Feng, H., Wang, C., and Ren, W., "On-chip photothermal gas sensor based on a lithium niobate rib waveguide," Sensors and Actuators B: Chemical 405, 135392 (2024).

[36] Zheng, K., Pi, M., Huang, Y., Peng, Z., Zhao, H., Bao, H., Jiang, S., Ho, H.L., Zheng, C., et al., "Waveguide-Based On-Chip Photothermal Spectroscopy for Gas Sensing," Laser & Photonics Reviews 18(5), 2301071 (2024).

[37] Ricchiuti, G., Walsh, A., Mendoza-Castro, J.H., Vorobev, A.S., Kotlyar, M., Lukasievicz, G.V.B., Iadanza, S., Grande, M., Lendl, B., et al., "Photothermal spectroscopy on-chip sensor for the measurement of a PMMA film using a silicon nitride micro-ring resonator and an external cavity quantum cascade laser," Nanophotonics 13(13), 2417–2427 (2024).

[38] Yi, Z., Hu, J., and Lin, H., "Double resonance 1-D photonic crystal cavities for single-molecule mid-infrared photothermal spectroscopy: theory and design," Optics Letters 37(8), 1304–1306 (2012).

[39] Puckett, M.W., Liu, K., Chauhan, N., Zhao, Q., Jin, N., Cheng, H., Wu, J., Behunin, R.O., Rakich, P.T., et al., "422 Million intrinsic quality factor planar integrated all-waveguide resonator with sub-MHz linewidth," Nature Communications 12, 934 (2021).

[40] Bauters, J.F., Heck, M.J.R., John, D., Dai, D., Tien, M.-C., Barton, J.S., Leinse, A., Heideman, R.G., Blumenthal, D.J., et al., "Ultra-low-loss high-aspect-ratio Si3N4 waveguides," Optics Express 19(4), 3163 (2011).

[41] Fahrenkopf, N.M., McDonough, C., Leake, G.L., Su, Z., Timurdogan, E., and Coolbaugh, D.D., "The AIM Photonics MPW: A Highly Accessible Cutting Edge Technology for Rapid Prototyping of Photonic Integrated Circuits," IEEE Journal of Selected Topics in Quantum Electronics 25(5), 8201406 (2019).

[42] Deenadayalan, V., Stievater, T.H., Tyndall, N.A., Fanto, M., Kozak, D.A., Pruessner, M.W., Rabinovich, W.S., and Preble, S., "Foundry-processed optomechanical photonic integrated circuits," OSA Continuum 4(4), 1215–1222 (2021).